Available online at www.sciencedirect.com
ScienceDirect
Journal of Power Sources 175 (2008) 806–816
JOURNAL OF POWER SOURCES
www.elsevier.com/locate/jpowsour

Review

Effects of internal flow modification on the cell performance enhancement of a PEM fuel cell

Shiang-Wuu Perng [a], Horng-Wen Wu [b,*]

[a] *Department of Accounting Information, Kun Shan University, No. 949 Da Wan Road, Yung-Kang City, Tainan Hsien 710, Taiwan, ROC*
[b] *Department of Systems and Naval Mechatronic Engineering, National Cheng Kung University, Tainan, Taiwan, ROC*

Received 17 July 2007; received in revised form 21 September 2007; accepted 21 September 2007
Available online 4 October 2007

Abstract

This study presents a numerical investigation on the cell performance enhancement of a proton exchange membrane fuel cell (PEMFC) using the finite element method (FEM). The cell performance enhancement in this study has been accomplished by the transverse installation of a baffle plate and a rectangular block for the modification of flow pattern in the flow channel of the fuel cell. The baffle plates (various gap ratios, $\lambda = 0.005$–10) and the rectangular block (constant gap ratio, $\lambda = 0.2$) are installed along the same gas diffusion layer (GDL) in the channel at constant Reynolds number for the purpose of investigating the cell performance. The results show that the transverse installation of a baffle plate and a rectangular block in the fuel flow channel can effectively enhance the local cell performance of a PEMFC. Besides, the effect of a rectangular block on the overall cell performance is more obvious than a baffle plate.

Keywords: PEMFC; Cell performance; Gap ratio; Internal flow modification

Contents

1. Introduction 807
2. Numerical modeling 808
   2.1. Governing equations 809
   2.2. The initial and boundary conditions 809
   2.3. Numerical methods 810
3. Results and discussion 810
   3.1. Model validation 810
   3.2. Influence of internal flow modification 811
   3.3. Polarization curve 814
4. Conclusions 815
   Acknowledgement 816
   References 816

* Corresponding author. Tel.: +886 6 2740718x223; fax: +886 6 2747019.
E-mail address: z7708033@email.ncku.edu.tw (H.-W. Wu).

0378-7753/$ – see front matter © 2007 Elsevier B.V. All rights reserved.
doi:10.1016/j.jpowsour.2007.09.095

Nomenclature

A	diffusion matrix of concentration equation
c_{H_2O}	dimensionless water vapor concentration (mol m^{-3})
c_{O_2}	dimensionless oxygen concentration (mol m^{-3})
$c_{O_2,ref}$	reference oxygen concentration at inlet (mol m^{-3})
$c^*_{H_2O}$	water vapor concentration
$c^*_{O_2}$	oxygen concentration
C	fluid concentration vector of nodal points
D	divergence matrix
D_{H_2O}	binary diffusivity of water vapor in the oxygen (m^2 s^{-1})
$D_{H_2O,eff}$	effective diffusivity of water vapor in the gas diffusion layer (m^2 s^{-1})
D_{O_2}	binary diffusivity of oxygen in the water vapor (m^2 s^{-1})
$D_{O_2,eff}$	effective diffusivity of oxygen in the gas diffusion layer (m^2 s^{-1})
Da	Darcy number
F	Faraday's constant (C mol^{-1})
H	flow channel height (mm)
H_1	gas diffusion layer thickness (mm)
H_2	gap size between the gas diffusion layer and the baffle plate (or the rectangular) (mm)
I	averaged current density on the catalyst surface (A m^{-2})
I_x	local current density along the catalyst surface (A m^{-2})
I_0	Exchange current density (A m^{-2})
K	conduction matrix
L	flow channel length (mm)
L_D	distance between top surfaces of cylinder and exit plane
L_U	distance between inlet plane and bottom surfaces of cylinder
L_1	length of the upstream region before a baffle plate or a rectangular block (mm)
L_2	width of a baffle plate or a rectangular block (mm)
L_3	length of the downstream region behind a baffle plate or a rectangular block (mm)
M	mass matrix
$\mathbf{M}_D$	diagonalized mass matrix
p	dimensionless pressure ($p^*/\rho_f u_{in}^2$)
p^*	pressure (N m^{-2})
P	pressure vector of nodal points
Q	imposition vector of concentration boundary conditions on the catalyst surface
R	universal gas constant (mol^{-1} K^{-1})
R_{M1}, R_{N1}	coefficients in Eqs. (18a) and (18b)
Re	Reynolds number ($u_{in}H/\nu$)
S	diffusion matrix of the momentum equation
Sc_i	Schmidt number ($Sc_{O_2} = \nu/D_{O_2,eff}$ for oxygen; $Sc_{H_2O} = \nu/D_{H_2O,eff}$ for water vapor)
t	dimensionless time ($t^*/(H/u_{in})$)
Δt	dimensionless time interval
t^*	time
T	operating temperature
u, v	dimensionless velocity components ($u = u^*/u_{in}$, $v = v^*/u_{in}$)
$\vec{u}$	dimensionless velocity vector
u_{in}	inlet average velocity
u^*, v^*	velocity components
$\vec{u}^*$	velocity vector
U	velocity vector of nodal points
$\hat{\mathbf{U}}$	intermediate velocity matrix
x, y	dimensionless x^*, y^* coordinates ($x = x^*/H$, $y = y^*/H$)
x^*, y^*	physical coordinates
Z	pressure gradient matrix

Greek symbols

ε	porosity of the gas diffusion layer
η	over-potential on the cathode side
κ	permeability of gas diffusion layer
λ	gap ratio ($\lambda = H_2/H$)
ν	fluid kinematic viscosity
ρ_f	fluid density
τ	tortuosity of the gas diffusion layer

Superscript

$n+1$, n, $n-1$ $n+1$th, nth, $n-1$th time step

1. Introduction

Fuel cell (FC) is an electrochemical system that converts the chemical energy from the reaction of a fuel (usually hydrogen) and an oxidant (usually oxygen in ambient air) directly into electricity with high efficiency and high environment compatibility. FC technology offers the prospect of zero emission energy production for applications ranging from stationary power generation for electric utilities networks to automotive transportation. Among several types of fuel cells, the proton exchange membrane fuel cell (PEMFC) operates at significantly low temperature (80–90 °C) than other types. It has been considered as a potential candidate of the power sources in the future; their potential has, for instance, been demonstrated in the Ballard transit bus [1].

Design of the flow channel in bipolar plates is one of the important factors for the cell performance of a PEMFC system. In the past, therefore, lots of studies have been endeavored to various flow channels in PEMFC systems such as the arrangements of serpentine channel, multiple channels in parallel type, and interdigited channels, and so on. The fuel flow channel has a gas diffusion layer (GDL) as a side-wall, so that the GDL morphology may influence the reactant gas transport from channel to the catalyst surface and the cell performance. The effects of the rib spacing of the fuel flow channels and the GDL thickness

on the cell performance were investigated by West and Fuller [2]. Gurau et al. [3] proposed a one-dimensional mathematical model of a PEMFC containing a cathode gas channel, a gas diffusion layer, a catalyst layer, and a membrane. Analytical solutions were derived for the coupled equations, consisting of the oxygen mass transport equation and Ohm's law for proton migration in a heterogeneous domain. Jordan et al. [4] explained the effects of the GDL morphology on the cell performance by conducting experiments with a model of hydrophobilicity. For the performance of a PEMFC, the cathode is regarded as the dominant component. This is due to the slow kinetics of oxygen reduction [5] and the cell performance depends strongly on the oxygen transport rate to the cathode. Therefore, the modeling of the cathodic half cell of a PEMFC has been emphasized [5–7].

Several papers [8–11] have dealt with the numerical computations to perform the flow distribution and fuel gas diffusion. Wang et al. [8] developed a two-dimensional numerical model to study the two-phase flow transport in the air cathode of a PEMFC. In this paper, the model encompassed both single- and two-phase regimes corresponding to low and high current densities and was capable of predicting the transition between the two regimes. Hontanon et al. [9] employed the Navier–Stokes equations and the Michaelis–Menten type two-step kinetics model to study the performance of the grooved plate and porous flow distributors at anode. The results showed that the fuel consumption increases with decreasing the permeability of the flow distributor. Also, they found that the porous materials are more advantageous than the grooved plates considering the reactant gas under the same pressure drop. Kee et al. [10] performed a generalized computational model for the mass and momentum transport in channel networks of typical planar fuel cell layers/stacks. Kumar and Reddy [11] studied numerically the flow field of the bipolar plates with metal foam in a PEMFC. These results revealed that the use of metal foam renders the local current density distribution more uniform.

Although many papers have been conducted on the enhancement of the cell performance of the PEMFC for various configurations of fuel flow channel, there are few reports on the influence of the blockage at various gap ratios and the comparison between the baffle plate and the rectangular block applied to the fuel flow channel. One of the enhancement techniques is to modify the flow pattern through the fact that more fuel gas in the flow channel can be forced into the gas diffusion layer. The enhancement technique investigated here is the employment of the baffle plate and the rectangular block to generate the blockage effect on the fuel flow in the channel. Examining the efficacy of the enhancement technique for the cell performance of a PEMFC is a motivation to us from practical consideration. The purpose of this paper is to quantify numerically the influence of a baffle plate on the cell performance enhancement by changing the gap ratio and to compare the enhancement between a baffle plate and a rectangular block installed in the fuel flow channel. According to the results of the references [12,13], the liquid water effect does not change the trend of fuel cell performance enhanced by the internal flow modification. In addition, from the references' discussion, the temperature effect on the fuel cell performance enhancement by means of the internal flow modification is slight. Therefore, the temperature and two-phase effects are neglected in the model to investigate the effects of internal flow modification on the cell performance enhancement of a PEMFC. Hwang et al. [14] investigated the effects of gas-distributor geometry and cathodic over-potential on the oxygen transport illustrated by the flow structure, oxygen concentration and current density distributions. This paper describes a semi-implicit finite element study that investigated flow modification by means of the blockage effect generated by the baffle plate or the rectangular block and its effects on the cell performance of a PEMFC when changing the cathodic over-potential. Semi-implicit finite element method with the projection technique proposed by Ramaswamy et al. [15,16] is a powerful numerical method for unsteady incompressible flows. They showed that this method generally requires much less computer storage and CPU time than the conventional finite element methods. The results of this paper may be of interest to engineers attempting to develop the optimization of a PEMFC and to researchers interested in the flow modification aspects of the PEMFC performance enhancement in the cathode.

2. Numerical modeling

The physical problem considered in this paper is the two-dimensional half-cell model of the PEMFC system for the fuel gas mass and momentum transport in the flow channel and the porous GDL at the cathode as shown in Fig. 1. The geometrical relations in this study are set forth: $H_1/H = 0.4$, $L/H = 20$, $L_1/H = L_3/H = 9.9$, $L_2/H = 0.2$. The dimensionless parameter named the gap ratio, $\lambda = H_2/H$, is defined to characterize the blockage effect of the baffle plate and the rectangular block. The gap ratio λ is equal to 1 for the block-free and zero for the fully blocked. Besides, the gap ratio λ is in the range from 0.005 to 0.2 for the baffle plate, and λ is set to be 0.2 for the rectangular

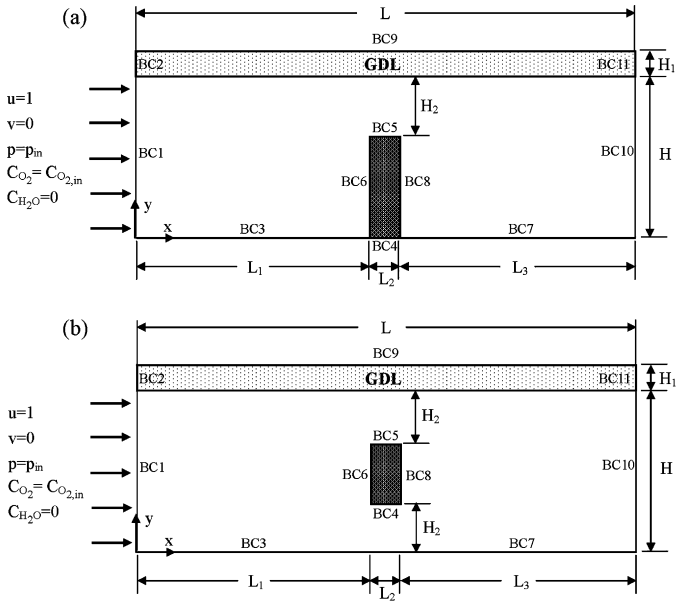

Fig. 1. The configuration of a PEMFC half cell in a flow channel: (a) with a baffle plate and (b) with a rectangular block.

block. The following assumptions are employed in the model of this study:

(1) Gas mixtures are ideal gases.
(2) The fluid flow is unsteady, laminar, and incompressible; all the physical properties of the fluid are taken to be constant.
(3) Porous GDL is homogeneous and isotropic with uniform morphological properties.
(4) Water in the electrode exists as vapor only.
(5) Catalyst layer is considered to be an ultra-thin layer, and thus the oxygen reduction reaction is considered to occur only on the surface of the catalyst layer.
(6) The fuel cell operates at a constant temperature of 353 K.

2.1. Governing equations

The two-dimensional governing equations for the fuel flow channel and gas diffusion layer in a half-cell of the PEMFC can be expressed as

$$\nabla \cdot (\rho_f \vec{u}^*) = 0 \tag{1}$$

$$\frac{\partial \vec{u}^*}{\partial t^*} + (\vec{u}^* \cdot \nabla)\vec{u}^* = -\frac{1}{\rho_f}\nabla p^* + \frac{\mu}{\rho_f}\nabla^2 \vec{u}^* - \frac{\mu}{\rho_f \kappa}\varepsilon \vec{u} \tag{2}$$

$$\frac{\partial c_i^*}{\partial t^*} + (\vec{u}^* \cdot \nabla)c_i^* = D_{i,\text{eff}}\nabla^2 c_i^* \tag{3}$$

where $\vec{u}^*$ is the velocity vector, p^* the pressure, ρ_f the fluid density, μ the fluid viscosity, c_i^* the fluid concentration and $D_{i,\text{eff}}$ the effective diffusivity. In addition, the effective diffusivity $D_{i,\text{eff}}$ is modified by the Bruggman correlation [17] in order to account for the effects of porosity and tortuosity (τ) in the porous electrode, i.e.,

$$D_{O_2,\text{eff}} = \varepsilon^\tau D_{O_2} \tag{4}$$

$$D_{H_2O,\text{eff}} = \varepsilon^\tau D_{H_2O} \tag{5}$$

The governing equations are normalized by first defining dimensionless independent variables of the form $x = x^*/H$, and $y = y^*/H$. Moreover, dependent dimensionless variables may also be defined as $\vec{u} = \vec{u}^*/u_{in}$, $t = t^* u_{in}/H$, $p = p^*/(\rho_f u_{in}^2)$, $Da = \kappa/H^2$, $Re = (u_{in}H)/\nu$, $c_i = c_i^*/c_{O_2,\text{ref}}$ and $Sc_i = \nu/D_{i,\text{eff}}$; the above governing equations can be expressed as the non-dimensional form:

$$\nabla \cdot \vec{u} = 0 \tag{6}$$

$$\frac{\partial \vec{u}}{\partial t} + (\vec{u} \cdot \nabla)\vec{u} = -\nabla p + \frac{1}{Re}\nabla^2 \vec{u} - \frac{1}{Re\,Da}\varepsilon \vec{u} \tag{7}$$

$$\frac{\partial c_i}{\partial t} + (\vec{u} \cdot \nabla)c_i = \frac{1}{Re\,Sc_i}\nabla^2 c_i \tag{8}$$

The momentum equations are valid in both the porous gas diffusion layer and the fuel flow channel. They are reduced to the extended Darcy's law for flow in the porous cathode with a small permeability [18], and become the Navier–Stokes equations inside the flow channel with the porosity of unity and the permeability of infinite.

2.2. The initial and boundary conditions

The initial conditions are prescribed for $t = 0$, in the region, $u = v = c_{O_2} = c_{H_2O} = 0$. We use the following boundary conditions for computations as shown in Fig. 1:

(a) At the oxygen inlet (BC1):

$$u = 1, \qquad v = 0, \qquad c_{O_2} = c_{O_2,\text{in}}, \qquad c_{H_2O} = 0 \tag{9}$$

(b) At the both sides of the GDL (BC2 and BC11):

$$u = v = \frac{\partial c_{O_2}}{\partial x} = \frac{\partial c_{H_2O}}{\partial x} = 0 \tag{10}$$

(c) On the left and right faces of the baffle plate and the rectangular block (BC6 and BC8):

$$u = v = \frac{\partial c_{O_2}}{\partial x} = \frac{\partial c_{H_2O}}{\partial x} = \frac{\partial p}{\partial x} = 0 \tag{11}$$

(d) On the current collector surfaces, the upper surface of the baffle plate, and the upper and lower surfaces of the rectangular block (BC3, BC4, BC5 and BC7):

$$u = v = \frac{\partial c_{O_2}}{\partial y} = \frac{\partial c_{H_2O}}{\partial y} = \frac{\partial p}{\partial y} = 0 \tag{12}$$

(e) At the outlet (BC10):

$$\frac{\partial u}{\partial x} = \frac{\partial v}{\partial x} = \frac{\partial c_{O_2}}{\partial x} = \frac{\partial c_{H_2O}}{\partial x} = \frac{\partial p}{\partial x} = 0 \tag{13}$$

(f) On the surface of the catalyst layer (BC9):

$$u = v = \frac{\partial p}{\partial y} = 0 \tag{14}$$

For the boundary conditions of the reactant concentrations on the surface of the catalyst layer, the Butler–Volmer correlation [19] was employed to describe the rate of electrochemical reaction on the surface by the relationship of the local current density and the reactant concentrations:

$$I_x = I_0 \left[\left(\frac{c_{O_2}^*}{c_{O_2,\text{ref}}} \right) \exp\left(\frac{4\alpha F}{RT}\eta \right) \right] \tag{15}$$

α is the electrochemical coefficients depending on the exchange current density and the over-potential on the electrode surfaces. In this study, it is considered to be constant. In Eq. (15), the first term is the reductive current representing the strength of forward reaction, while the second term is the oxidative current that has an opposed effect on the oxygen reduction reaction (ORR). According to $O_2 + 4H^+ + 4e^- \leftrightarrow 2H_2O$, the oxygen consumed rate on the reaction surfaces by the ORR should be equal to the produced current. Therefore, the balance of oxygen concentration on the reaction boundary becomes

$$-D_{O_2,\text{eff}}\frac{\partial c_{O_2}^*}{\partial y^*} = \frac{I_x}{4F} \tag{16a}$$

$$D_{H_2O,\text{eff}}\frac{\partial c_{H_2O}^*}{\partial y^*} = \frac{I_x}{2F} \tag{16b}$$

According to Eqs. (15) and (16), we can obtain the following equations:

$$D_{O_2,\text{eff}}\frac{\partial c^*_{O_2}}{\partial y^*} + \frac{I_0}{4F}\left(\frac{c^*_{O_2}}{c_{O_2,\text{ref}}}\right)\exp\left(\frac{4\alpha F}{RT}\eta\right) = 0 \tag{17a}$$

$$D_{H_2O,\text{eff}}\frac{\partial c^*_{H_2O}}{\partial y^*} + \frac{I_0}{2F}\left(\frac{c^*_{O_2}}{c_{O_2,\text{ref}}}\right)\exp\left(\frac{4\alpha F}{RT}\eta\right) = 0 \tag{17b}$$

During the non-dimensional process, the non-dimensional boundary conditions can be written as:

$$\frac{\partial c_{O_2}}{\partial y} + R_{M1}c_{O_2} = 0 \tag{18a}$$

$$\frac{\partial c_{H_2O}}{\partial y} + R_{N1}c_{O_2} = 0 \tag{18b}$$

where the non-dimensional parameters described as follows:

$$R_{M1} = \frac{I_0 H\exp((4\alpha F/RT)\eta)}{4Fc_{O_2,\text{ref}}D_{O_2,\text{eff}}} \tag{19a}$$

$$R_{N1} = \frac{I_0 H\exp((4\alpha F/RT)\eta)}{2Fc_{O_2,\text{ref}}D_{H_2O,\text{eff}}} \tag{19b}$$

2.3. Numerical methods

Applying the standard Galerkin finite element to the spatial discretization of Eqs. (6)–(8) leads to the following systems of the coupled ordinary equations [15,16]:

$$\mathbf{M}\frac{\mathrm{d}\mathbf{U}}{\mathrm{d}t} + \mathbf{ZP} + \frac{1}{Re}\mathbf{S}(\mathbf{U}) + \boldsymbol{K}(\boldsymbol{U})\boldsymbol{U} = -\frac{\varepsilon}{Re\,Da}\boldsymbol{M}\boldsymbol{U}\delta_{i1} \tag{20}$$

$$\mathrm{M}\frac{\mathrm{d}\mathbf{C}}{\mathrm{d}t} + \frac{1}{Re\,Sc_i}\boldsymbol{A}\boldsymbol{C} + \boldsymbol{K}(\boldsymbol{U})\boldsymbol{C} = \frac{1}{Re\,Sc_i}\boldsymbol{Q} \tag{21}$$

$$\boldsymbol{D}\boldsymbol{U} = 0 \tag{22}$$

where **M** is the mass matrix, **K** the pressure gradient matrix, **Z** the convection matrix, and $\mathbf{D} = \mathbf{Z}^{\mathrm{T}}$ the divergence matrix. **S** is the diffusion matrix of the momentum equation, and **A** is the diffusion matrix of the concentration equations. Vectors **U**, **C**, and **P** represent finite element solutions of velocity, concentration, and pressure, respectively. The right hand side vector Q results from the imposition of the concentration boundary conditions on catalyst layer surface.

By adopting a second-order Adams–Bashforth scheme for the advection terms and an implicit Euler representation for the diffusion term, we may derive the finite element version of the semi-implicit projection scheme as follows [15]:

Step 1: Advection and viscosity phase. In this phase, the intermediae velocity field $\hat{\mathbf{U}}^{n+1}$ is found from $\mathbf{U}^n$ beginning with $\mathbf{U}_0$ for $n=0$, using the explicit Adams–Bashforth method for the nonlinear convection terms and a first-order implicit Euler time integration scheme for the diffusion term:

$$\boldsymbol{M}\hat{\boldsymbol{U}}^{n+1} = \boldsymbol{M}\boldsymbol{U}^n - \Delta t\left[\frac{3}{2}\boldsymbol{K}(\boldsymbol{U}^n)\boldsymbol{U}^n - \frac{1}{2}\boldsymbol{K}\boldsymbol{U}^{n-1}\boldsymbol{U}^{n-1}\right] - \frac{\Delta t}{\mathrm{Re}}\boldsymbol{S}(\boldsymbol{U}^{n+1}) - \frac{\Delta t\varepsilon}{\mathrm{Re\,Da}}\boldsymbol{M}\boldsymbol{U}^{n+1}\delta_{i1} \tag{23}$$

Step 2: Pressure phase. The phase allows us to determine final velocity $\mathbf{U}^{n+1}$ from intermediate velocity $\hat{\mathbf{U}}^{n+1}$ by adding the dynamic effect of the pressure $\mathbf{P}^{n+1}$ so that the incompressibility condition stays satisfied. This leads to the Poisson equation:

$$\mathbf{A}\mathbf{P}^{n+1} = \frac{1}{\Delta t}\mathbf{D}\hat{\mathbf{U}}^{n+1} \tag{24}$$

The final velocity is consequently computed:

$$\boldsymbol{M}_{\mathrm{D}}\boldsymbol{U}^{n+1} = \boldsymbol{M}_{\mathrm{D}}\hat{\boldsymbol{U}}^{n+1} - \Delta t\boldsymbol{Z}\boldsymbol{P}^{n+1} \tag{25}$$

where $\mathbf{M}_{\mathrm{D}}$ is the diagonalized mass matrix obtained simply by summing across each row of the consistent mass matrix and placing the results in the diagonal.

Step 3: Concentration phase. In the last phase, the concentration $\mathbf{C}^{n+1}$ is found by the concentration equation as the way in the velocity phase is derived:

$$\boldsymbol{M}\boldsymbol{C}^{n+1} = \boldsymbol{M}\boldsymbol{C}^n - \Delta t\left[\frac{3}{2}\boldsymbol{K}\boldsymbol{U}^n\boldsymbol{C}^n - \frac{1}{2}\boldsymbol{K}\boldsymbol{U}^{n-1}\boldsymbol{C}^{n-1}\right] - \frac{\Delta t}{Re\,Sc_i}\boldsymbol{A}(\mathbf{C}^{n+1}) + \frac{\Delta t}{Re\,Sc_i}\boldsymbol{Q}^n \tag{26}$$

The element mass, convection, pressure gradient, divergence, and diffusion matrices are calculated only once and used again at each time step. The skyline method was employed to reduce the storage of global matrices. A direct solver of LU factorization based on Gaussian elimination technique was developed to deal with a symmetric banded system.

3. Results and discussion

3.1. Model validation

For the baffle plate (the cathodic over-potential, $\eta = 0.1$–0.9) at constant Reynolds number ($Re = 15$), the gap ratio (λ) is changed by 0, 0.005, 0.025, 0.1 and 0.2 to investigate the blockage effect of the baffle plate on the enhancement of cell performance of a PEMFC. The geometric and physical parameters used in the present study are listed in Table 1. Furthermore, we will compare the performance enhancement between the baffle plate and the rectangular block installed in the fuel flow channel. After a series of mesh sensitivity tests for three finite-element meshes (9518 nodes and 9166 elements, 12,362 nodes and 12,060 elements, 14,958 nodes and 14,592 elements), the calculation results are indicated in Fig. 2(a). The local current density difference between the second and the third mesh was less than 0.05% in test runs, so a finite-element mesh (12,362 nodes and 12,060 elements) was chosen in all cases. The three time steps 0.00025, 0.0005, and 0.001 were chosen to test the time step size sensitivity. According to the results in Fig. 2(b), the time increment Δt was set at 0.0005 for all cases. In this study, about 80,000 time steps were necessary to obtain reasonably, reliable data. The CPU time was varied from 6 h 35 min 43 s to 7 h 21 min 13s in a PENTIUM III 1G PC.

In order to show that the program in this study can handle the cell performance of a PEMFC, we apply the present method to solve the oxygen gas transport through the cathode region of

Table 1
Geometric and physical parameters used in this study

Quantity	Value
Flow channel length, L (mm)	10
Flow channel height, H (mm)	0.5
Gas diffusion layer thickness, H_1 (mm)	0.2
Baffle plate width or rectangular block width, L_2 (mm)	0.1
Channel length before the baffle plate or the rectangular block, L_1 (mm)	4.95
Channel length behind the baffle plate or the rectangular block, L_3 (mm)	4.95
Operating temperature, T (K)	353
Operating pressure (atm)	1
Faraday constant, F (C mol^{-1})	96,487
Permeability of gas diffusion layer, κ (m^2)	1.0×10^{-12}
Universal gas constant, R (mol^{-1} K^{-1})	8.314
Open circuit voltage, V_{oc} (V)	1.1
Electrochemical coefficients, α	0.5
Porosity of the gas diffusion layer, ε	0.4
Tortuosity of the gas diffusion layer, τ	1.5
Inlet average velocity, u_{in} (m s^{-1})	0.25
Relatively humidity of inlet oxygen	0%
Exchange current density, I_0 (A m^{-2})	100
Reference oxygen concentration at inlet, $c_{O_2,ref}$ (mol m^{-3})	35.7
Fluid viscosity, μ (kg cm^{-1} s^{-1})	0.21×10^{-6}

a PEMFC as described in Kazim and others' paper [19]. The physical parameters and properties of the electrode are listed in Fig. 3. The mesh employed for the comparison with the reference was 4280 nodes and 3985 elements. The steady-state solution is obtained by the numerical procedure as mentioned in the previous section. As shown in Fig. 3, the result of the present predictions of the polarization curve agreeing fairly closely with Kazim and others' predictions [19] gives one confidence in the use of the present program.

3.2. Influence of internal flow modification

The local current density will be employed below to realize the influence of internal flow modification on the fuel cell performance in all cases at various gap ratios in this study. The local current density along the catalyst layer for the steady state is calculated by Eq. (16a) about 80,000 time steps. In Fig. 4 (overpotential η is equal to 0.4), except for the peak regions, the local current density along the catalyst surface decreases when the axial direction x increases. Besides, the local current density around the baffle plate or the rectangular block increases with increasing the blockage effect (decreasing λ values), and the difference of the peak regions between the baffle plate ($\lambda = 0.2$) and the rectangular block ($\lambda = 0.2$) is very small. These peak regions of the distribution of the local current density are caused by the transverse installation of a baffle plate and a rectangular block. This phenomena means that better cell performance is generated around the baffle plate or the rectangular block. This is due to the fact that the fuel gas is blocked by the baffle plate or the rectangular block installed in the flow channel, and

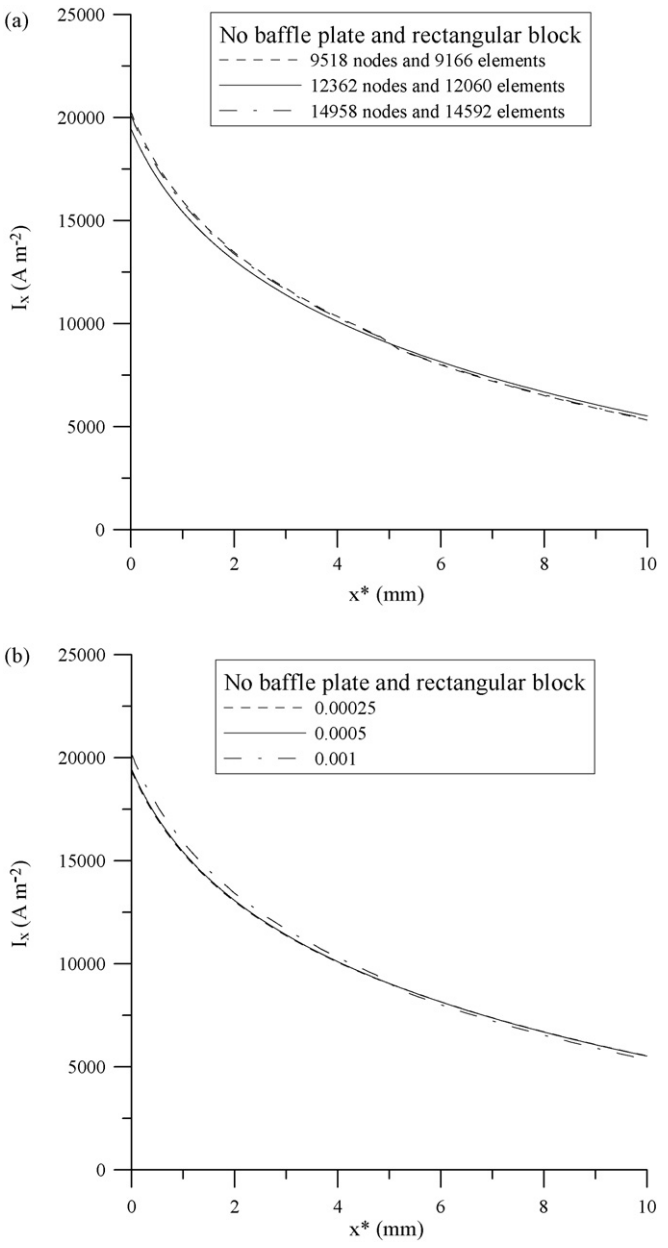

Fig. 2. (a) Grid sensitivity and (b) time step size sensitivity of local current density distribution on the surface of the catalyst layer for no baffle plate and rectangular block.

more fuel gas is forced into and passes through the gas diffusion layer (GDL), which enhances the chemical reaction on the catalyst surface. For the baffle plate or the rectangular block, the maximum local current density occurs at the front corner. In the upstream region before the baffle plate and the rectangular block, the local current density increases slightly by installing the baffle plate and the rectangular block; moreover, the rectangular block enhances the local current density better than the baffle plate. In the downstream region behind the baffle plate, the local current density decreases as the gap ratio λ decreases. The reduction of the local current density is a reflection of the more efficient fuel transport and the chemical reaction above the baffle plate but less flow into the GDL in the downstream region behind

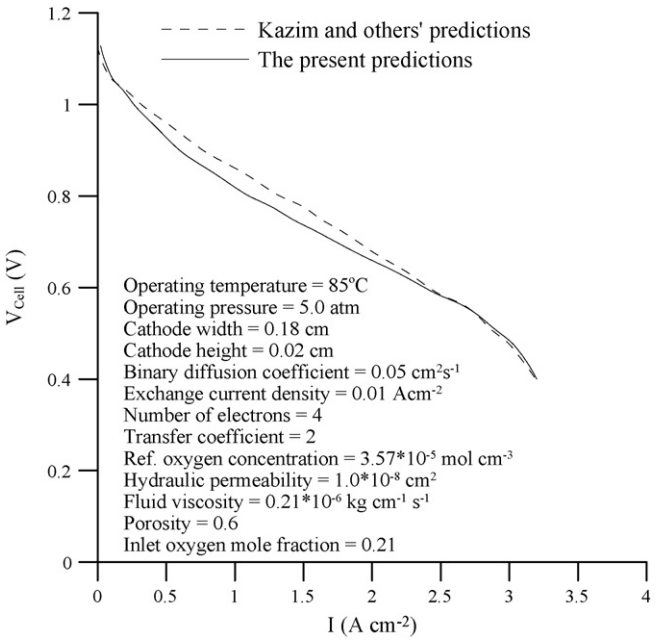

Fig. 3. Comparison of the results between the present prediction and Kazim and other's prediction.

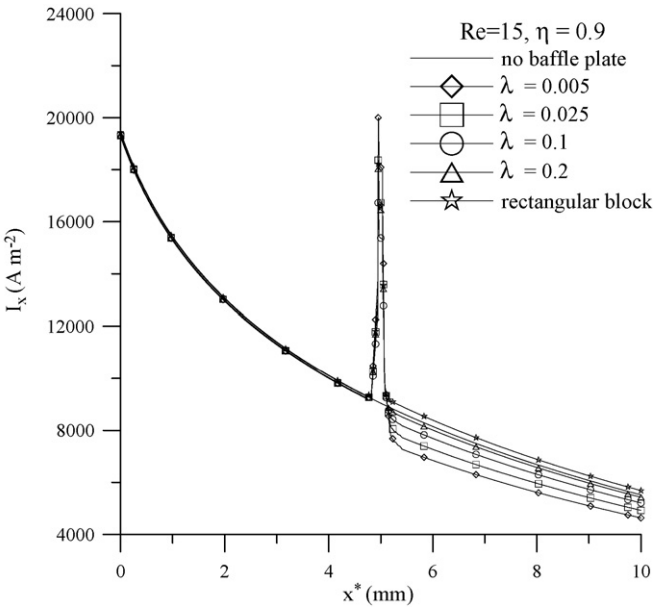

Fig. 5. The local current density distributions along the catalyst surface for different channel geometries at $Re = 15$ and $\eta = 0.9$.

the baffle plate. However, for the rectangular block, the above reflection disappears because the fuel gas can flow through the passageway between the rectangular block and the current collector surfaces. Therefore, the local current density increases by the installation of the rectangular block in the downstream. At a higher over-potential condition ($\eta = 0.9$, Fig. 5), the local current density along the catalyst surface decreases along the axial location, and the trend of the local current density distribution around the baffle plate or the rectangular block is similar to that as shown in Fig. 4. In Fig. 5, the distributions of the local current density are almost the same in the upstream region before the baffle plate and the rectangular block. The reduction of the local current density is more at $\eta = 0.9$ than $\eta = 0.4$ because the reflection phenomena becomes more obviously in the downstream region behind the baffle plate for the higher over-potential condition. In contrast, the local current density for the rectangular block increases without the reflection phenomena but due to the internal flow modification.

Fig. 6 indicates the influence of the internal flow modification on the axial distribution of oxygen mass flux along the catalyst surface. The oxygen decreases generally along the catalyst (with

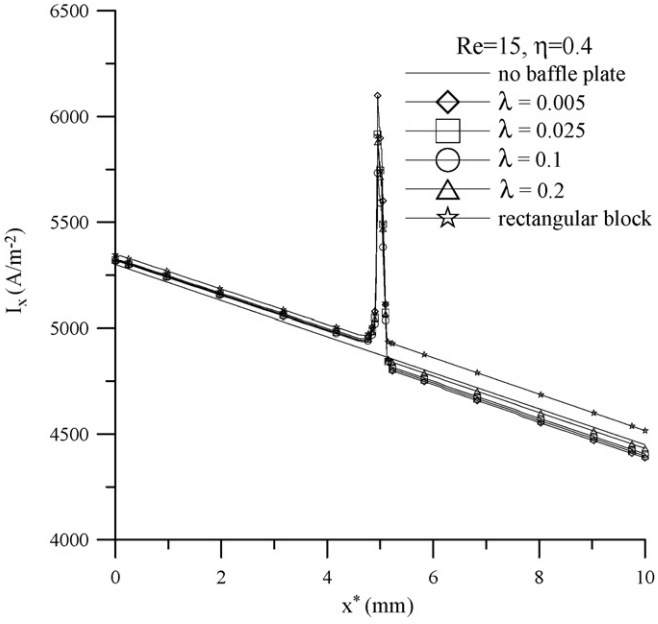

Fig. 4. The local current density distributions along the catalyst surface for different channel geometries at $Re = 15$ and $\eta = 0.4$.

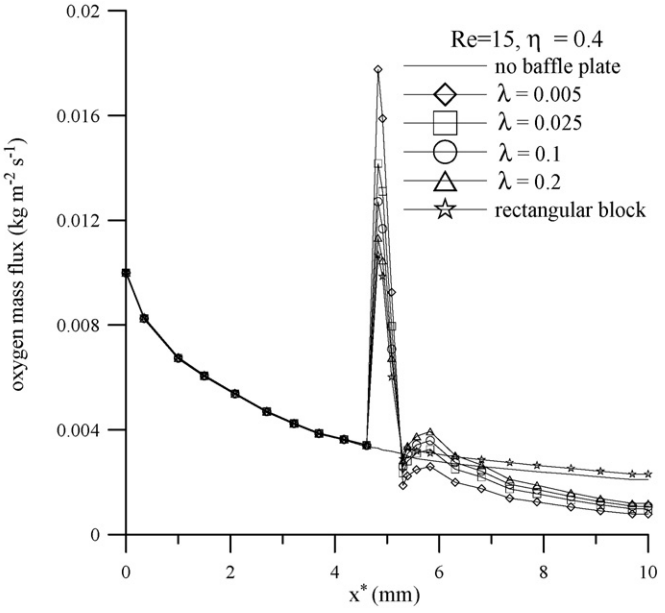

Fig. 6. The local distributions of oxygen mass fluxes along the catalyst surface for different channel geometries at $Re = 15$ and $\eta = 0.4$.

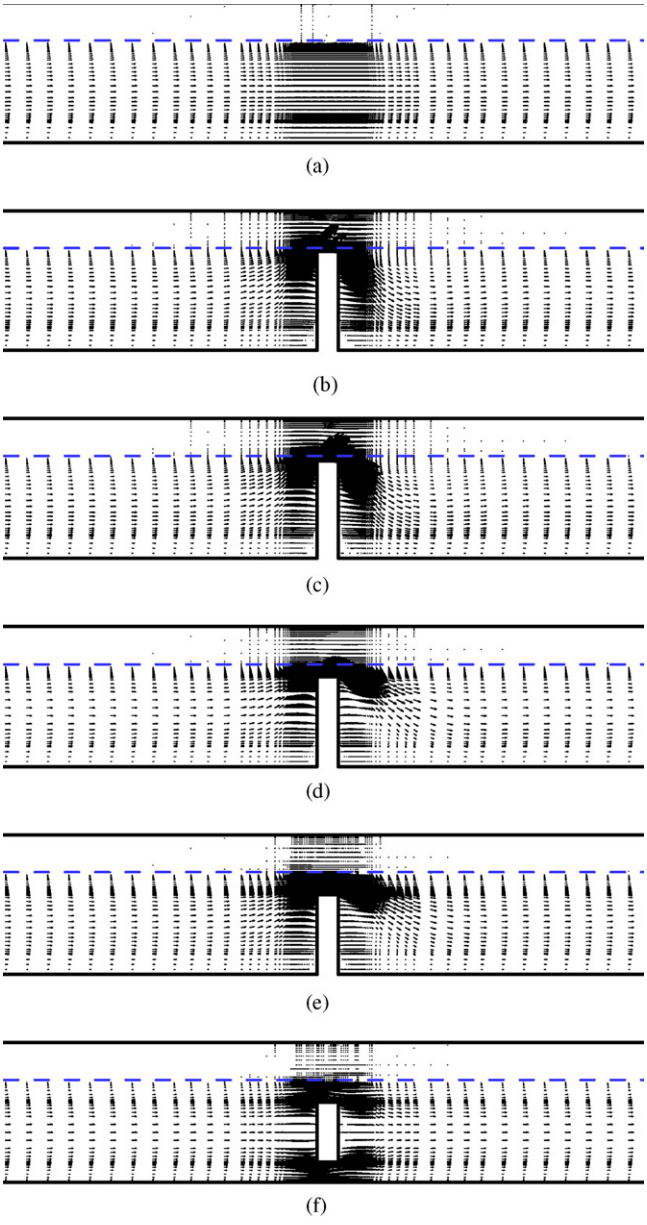

Fig. 7. The local distributions of velocity vectors for different channel geometries at $Re = 15$ and $\eta = 0.4$: (a) no baffle plate, (b) $\lambda = 0.005$, (c) $\lambda = 0.025$, (d) $\lambda = 0.1$, (e) $\lambda = 0.2$, (f) rectangular block.

an increase in the axial coordinate (x), but a hump region occurs around the location of the baffle plate or the rectangular block. This hump region is caused by the strong forced convection, which enhances the transport of oxygen. The peak of the hump region is raised when the gap ratio λ decreases. In the upstream before the baffle plate and the rectangular block, the oxygen mass fluxes almost have the same profiles. However, behind the baffle plate, the oxygen mass flux decreases with a decrease in λ because the stronger chemical reaction with fuel gas depletion occurs around the baffle plate. For the rectangular block, the oxygen mass flux becomes more than other cases because the oxygen can flow through the passageway between the current collector and the rectangular block. These results in Fig. 6 give one confidence in the results of Figs. 4 and 5.

The velocity fields in the region between the baffle plate (or the rectangular block) and the catalyst layer clearly demonstrate the oxygen mass flow rate through the gas diffusion layer. Fig. 7 illustrates the local distributions of the velocity vectors for various channel geometries at $Re = 15$ and $\eta = 0.4$. In Fig. 7(a), the gas flow moves downstream mainly through the passage between the GDL and the current collector, but little gas exists in the GDL at a lower porosity ($\varepsilon = 0.4$). By the transverse installation of a baffle plate and a rectangular block in the fuel flow channel, the gas flow can be forced into the GDL. The narrower gap makes more gas flow move into the gas diffusion layer, but deflects the gas flow out of the GDL behind the baffle plate downward more. The deflecting effect arising from the gas flow out of the GDL causes that the gas flow moves hard into the GDL in the down-

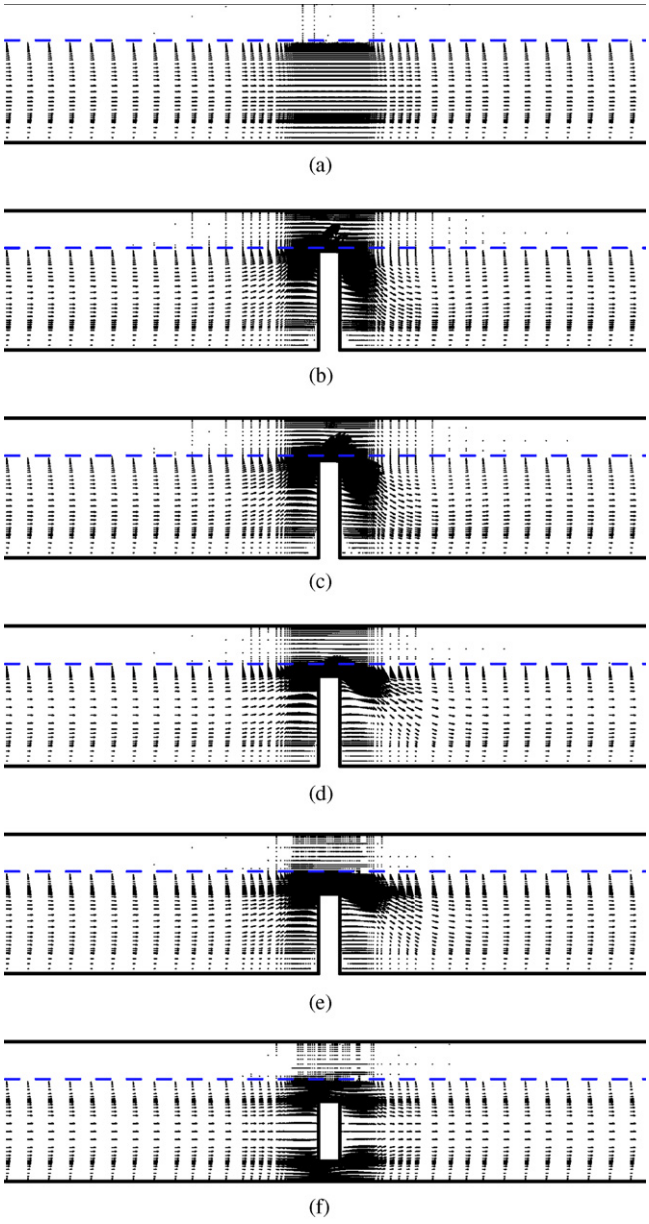

Fig. 8. The local distributions of velocity vectors for different channel geometries at $Re = 15$ and $\eta = 0.9$: (a) no baffle plate, (b) $\lambda = 0.005$, (c) $\lambda = 0.025$, (d) $\lambda = 0.1$, (e) $\lambda = 0.2$, (f) rectangular block.

stream behind the baffle plate. The deflecting effect also reduces the local current density in the downstream region behind the baffle plate as shown in Figs. 4 and 5. In order to consider the more gas flow forced into the GDL and to reduce the deflecting effect, the rectangular block is in place of the baffle plate. In Fig. 7(f), the gas flow can be forced into the GDL by the gap between the GDL and the block, and the deflecting effect arising from the gas flow out of the GDL can be reduced by the gas flow through the passageway between the current collector and the block. These flow characteristics may be related to the pressure drop of the channel flow. At a higher over-potential ($\eta = 0.9$, Fig. 8), the distributions of the velocity vectors for various channel geometries are almost the same as the ones at a lower over-potential ($\eta = 0.4$, Fig. 7). This result shows that the change of the over-potential almost has no influence on the profiles of the velocity in the fuel flow channel.

In this paper, the model is considered to be the half cell on the cathode side, where the oxygen and the water vapor exist. In order to comprehend the influence of the internal flow modification on the cell performance, the distributions of oxygen have to be observed. Fig. 9 reveals the influence of various channel geometries on the contours of oxygen concentrations, but only shows the local profiles of the oxygen concentrations for understanding clearly. In Fig. 9, the oxygen concentration decreases along the channel length, and some oxygen enters the gas diffusion layer. By installing the baffle plate or the rectangular block (Fig. 9 (b)–(f)), a large amount of oxygen is forced to move into the porous GDL around the region on the baffle plate or the rectangular block, and a strong reaction and higher consumption of oxygen occur in this region. Besides, the narrower gap (smaller λ) makes more oxygen move locally into the porous GDL around the region on the baffle plate, but causes the larger area of low oxygen concentrations in the downstream region behind the baffle plate. The smaller λ leads to a higher reaction rate locally on the catalyst surface and therefore a local better cell performance around the region on the baffle plate, but a lower reaction rate and a worse cell performance in the downstream region behind the baffle plate. For the rectangular block (Fig. 9(f)), the gap between the block and the GDL makes oxygen move into the porous GDL; furthermore, the oxygen can flow through the passageway between the block and the current collector. Therefore, the area of low oxygen concentrations is smaller than other cases in the downstream region behind the baffle plate. This means that installing the rectangular block obtains a better cell performance than other cases in the overall PEMFC system. Fig. 10 shows the local distributions of oxygen concentration for various geometries at a higher over-potential ($\eta = 0.9$). According to the comparison of oxygen concentration profile between Figs. 9 and 10, a higher over-potential gets a higher oxygen concentration profile in the flow channel and in the porous GDL. This characteristic of oxygen concentration profiles leads to a higher reaction rate and a better overall cell performance at $\eta = 0.9$ than at $\eta = 0.4$. In Fig. 10, the distributions of oxygen concentration for various channel geometries have the same trend as the distributions of oxygen concentration presented in Fig. 9, and thus the over-potential value almost has little influence on the trend of oxygen concentration profiles for

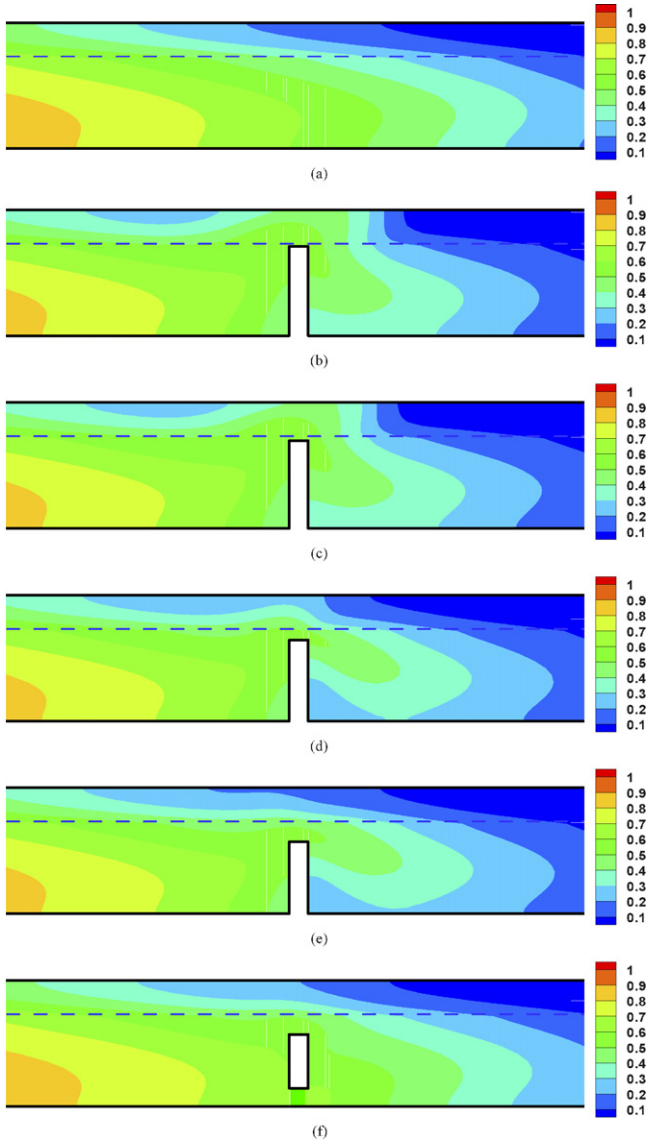

Fig. 9. The local distributions of dimensionless oxygen concentration for different channel geometries at $Re = 15$ and $\eta = 0.4$: (a) no baffle plate, (b) $\lambda = 0.005$, (c) $\lambda = 0.025$, (d) $\lambda = 0.1$, (e) $\lambda = 0.2$, (f) rectangular block.

various channel geometries. From these distributions of oxygen concentrations as shown in Figs. 9 and 10, except for the regions around the baffle plate and in the downstream behind the baffle plate, the oxygen profiles along the catalyst surface have little variations with different channel geometries. This phenomenon can interpret the local current density distributions along the catalyst surface as shown in Figs. 4 and 5.

3.3. Polarization curve

The purpose of this paper is to quantify numerically the influence of a baffle plate on the cell performance enhancement by changing the gap ratio and to compare the enhancement between a baffle plate and a rectangular block. The overall cell performance of a PEMFC system is understood clearly by means of plotting the polarization curve. In the polarization curves, the abscissa is the averaged current density on the catalyst surface

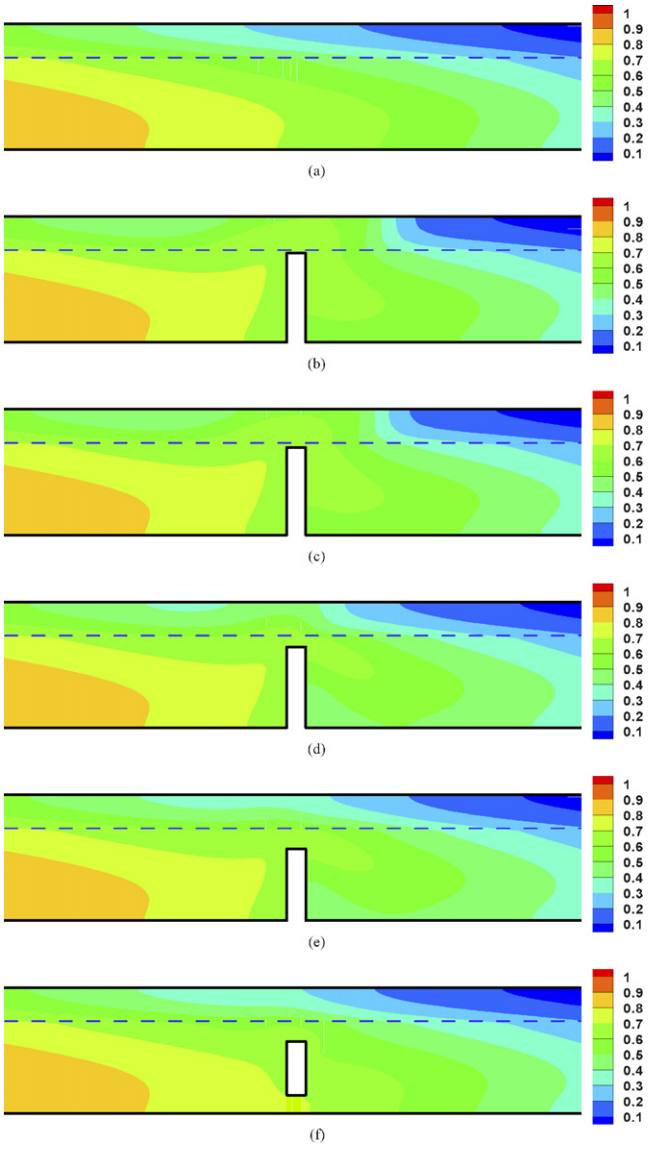

Fig. 10. The local distributions of dimensionless oxygen concentration for different channel geometries at $Re = 15$ and $\eta = 0.9$: (a) no baffle plate, (b) $\lambda = 0.005$, (c) $\lambda = 0.025$, (d) $\lambda = 0.1$, (e) $\lambda = 0.2$, (f) rectangular block.

and the ordinate is the fuel cell potential. The averaged current density on the catalyst surface is determined by:

$$I = \frac{1}{L}\int_0^L I_x \, \mathrm{d}x \tag{27}$$

Furthermore, neglecting the over-potential on the anode side, the fuel cell potential (the operating voltage) is calculated as:

$$V_{\mathrm{cell}} = V_{\mathrm{oc}} - \eta \tag{28}$$

where V_{oc} is the open circuit voltage kept constant, and the value of V_{oc} is listed in Table 1; η is the over-potential on the cathode side. Fig. 11 illustrates the polarization curves of the fuel cell performance for different channel geometries to investigate the influence of the internal flow modification on the overall fuel cell performance. An overall inspection of Fig. 11 indicates that at the conditions of the higher operating voltage (lower over-

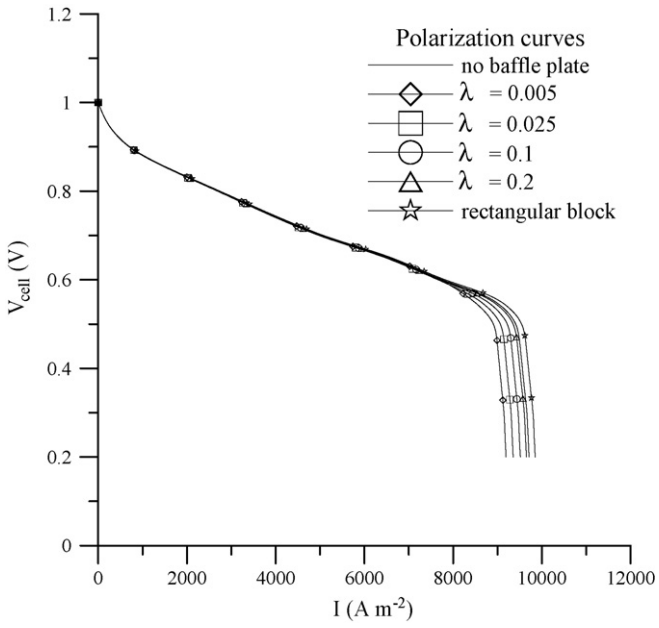

Fig. 11. The polarization curves of the fuel cell performance for different channel geometries at $Re = 15$.

potential on the cathode side), the influence of the internal flow modification on the overall fuel cell performance is negligibly small as compared with those without a baffle plate or a rectangular block. At lower operating voltage conditions, on the other hand, the effect of the internal flow modification on the polarization curves becomes important. In addition, for the installation of a baffle plate, the overall cell performance decreases when the gap ratio λ decreases. This is due to the fact that a reflection of the more efficient fuel transport and the chemical reaction around the baffle plate reduces the local current density more obviously in the downstream region behind the baffle plate as described previously in Figs. 4 and 5. The installation of a rectangular block has better overall cell performance than the installation of a baffle plate and enhances the overall cell performance of a PEMFC system, because the above reflection disappears with the fuel gas through the passageway between the rectangular block and the current collector surfaces. From these results, the next studies are going to increase the width and numbers of baffle plate or rectangular block for the purpose of enlarging the blockage area so as to enhance the overall fuel cell performance.

4. Conclusions

A finite element analysis of the cell performance enhancement has been accomplished by the transverse installation of a baffle plate and a rectangular block for the internal flow modification in the fuel flow channel. The results of the polarization curve computed in this paper are in good agreement with those of other predictions. Both better local cell performance and gas reactant transport are generated around the baffle plate or the rectangular block when the blockage effect increases (decreasing λ values). Both worse local cell performance and gas reactant transport occur in the downstream region behind the baffle plate with an increase in the blockage effect (decreasing λ values)

while the local cell performance is enhanced in the downstream region behind the rectangular block.

A higher over-potential obtains a higher oxygen concentration profile in the flow channel and in the porous GDL, and then leads to a higher reaction rate and a better overall cell performance. For the baffle plate, the local current density reduces more obviously at a higher over-potential than at a lower over-potential because of the more obvious reflection phenomena in the downstream region. At lower operating voltage conditions, the overall cell performance decreases as the gap ratio λ decreases for a baffle plate; however, the installation of a rectangular block has better overall cell performance than the installation of a baffle plate and enhances the overall cell performance of a PEMFC system.

Acknowledgement

The authors gratefully acknowledge the partial financial support of this project by the National Council of the Republic of China.

References

[1] K.B. Prater, J. Power Sources 37 (1992) 181–188.
[2] A.C. West, T.F. Fuller, J. Appl. Electrochem. 26 (6) (1996) 557–565.
[3] V. Gurau, F. Barbir, H. Liu, J. Electrochem. Soc. 147 (7) (2000) 2468–2477.
[4] L.R. Jordan, A.K. Shukla, T. Behrsing, N.R. Avery, B.C. Muddle, M. Forsyth, J. Power Sources 86 (2000) 250–254.
[5] T.E. Springer, T.A. Zawodzinski, S. Gottesfeld, J. Electrochem. Soc. 138 (8) (1991) 2334–2342.
[6] J.S. Yi, T.V. Nguyen, J. Electrochem. Soc. 146 (1) (1999) 38–45.
[7] A. Kazim, H.T. Liu, P. Forges, J. Appl. Electrochem. 29 (12) (1999) 1409–1416.
[8] Z.H. Wang, C.Y. Wang, K.S. Chen, J. Power Sources 94 (1) (2001) 40–50.
[9] E. Hontanon, M.J. Escudero, C. Bautista, P.L. Garcia-Ybarra, L. Daza, J. Power Sources 86 (1–2) (2000) 363–368.
[10] R.J. Kee, P. Korada, K. Walters, M. Pavol, J. Power Sources 109 (1) (2002) 148–159.
[11] A. Kumar, R.G. Reddy, J. Power Sources 114 (1) (2003) 54–62.
[12] C.Y. Soong, W.M. Yan, C.Y. Tseng, H.C. Liu, F. Chen, H.S. Chu, J. Power Sources 143 (2005) 36–47.
[13] H.C. Liu, W.M. Yan, C.Y. Soong, F. Chen, H.S. Chu, J. Power Sources 158 (2006) 78–87.
[14] J.J. Hwang, C.K. Chen, R.F. Savinell, C.C. Liu, J. Wainright, J. Appl. Electrochem. 34 (2004) 217–224.
[15] B. Ramaswamy, T.C. Jue, J.E. Akin, Int. J. Numer. Methods Eng. 34 (1992) 675–696.
[16] B. Ramaswamy, T.C. Jue, Int. J. Numer. Methods Eng. 35 (1992) 671–707.
[17] R.E. Meredith, C.W. Tobias, in: C.W. Tobias (Ed.), Advances in Electrochemistry and Electrochemical Engineering, vol. 2, Interscience Publishers, New York, 1962.
[18] D.M. Bernardi, M.W. Verbrugge, AIChE J. 37 (8) (1991) 1151–1163.
[19] A. Kazim, P. Forges, H.T. Liu, Int. J. Energy Res. 27 (4) (2003) 401–414.